Composites Part B 315 (2026) 113503

Contents lists available at ScienceDirect

Composites Part B

journal homepage: www.elsevier.com/locate/compositesb

Functionalized two-dimensional carbon fillers for enhancing Li^+ conduction and interface stability of solid electrolyte for lithium batteries

Ananya Panda [a], Jui-Cheng Kao [a,b], Jagabandhu Patra [a,c], Chun-Wei Pao [b], Chun-Chen Yang [d,*], Chien-Te Hsieh [e], Fu-Ming Wang [f], Wei-Ren Liu [g], Ju Li [h], Ching-Yuan Su [i,**], Yu-Chieh Lo [a,***], Jeng-Kuei Chang [a,c,g,j,****]

[a] Department of Materials Science and Engineering, National Yang Ming Chiao Tung University, 1001 University Road, Hsinchu, 30010, Taiwan
[b] Research Center for Applied Sciences, Academia Sinica, No. 128, Section 2, Academia Road, Taipei, 11529, Taiwan
[c] Center for Resilience and Intelligence on Sustainable Energy Research (RiSER), National Cheng Kung University, 1 University Road, Tainan, 70101, Taiwan
[d] Battery Research Center of Green Energy, Ming Chi University of Technology, 84 Gongzhuan Road, New Taipei City, 243303, Taiwan
[e] Department of Chemical Engineering and Materials Science, Yuan Ze University, 135 Yuandong Road, Taoyuan, 32003, Taiwan
[f] Graduate Institute of Applied Science and Technology, National Taiwan University of Science and Technology, No. 43, Section 4, Keelung Road, Taipei, 106335, Taiwan
[g] Department of Chemical Engineering and R&D Center for Membrane Technology, Chung Yuan Christian University, 200 Chung Pei Road, Taoyuan, 32023, Taiwan
[h] Department of Nuclear Science and Engineering and Department of Materials Science and Engineering, Massachusetts Institute of Technology, 77 Massachusetts Avenue, Cambridge, MA, 02139, USA
[i] Institute of Energy Engineering, National Central University, 300 Jhong-Da Road, Taoyuan, 32001, Taiwan
[j] Sustainable Electrochemical Energy Development (SEED) Center, National Taiwan University of Science and Technology, No. 43, Section 4, Keelung Road, Taipei City, 106, Taiwan

ARTICLE INFO

Keywords:
Fluorinated graphene oxide
Two-dimensional fillers
Composite solid electrolyte
Density functional theory calculations
Interface stability

ABSTRACT

Solid-state Li-metal batteries (SSLMBs) are attractive for their safety and high energy density characteristics, enabled by solid-state electrolytes (SSEs) and lithium metal anodes. However, SSEs face challenges in ionic conductivity and interfacial stability. Herein, we develop composite solid electrolytes (CSEs) incorporating functionalized 2D graphene-based fillers, such as reduced graphene oxide, graphene oxide, and fluorinated graphene oxide (FGO), into a solid polymer electrolyte for $LiNi_{0.8}Co_{0.1}Mn_{0.1}O_2$ (NCM-811)-based SSLMBs. Among them, FGO exhibits the best performance, offering superior ionic conductivity (9.4×10^{-4} S cm^{-1} at 25 °C), a high Li^+ transference number (0.60), and a wide electrochemical window (~4.8 V). The Li^+ transport behavior in the CSEs with various functionalized graphene materials is examined via density functional theory calculations. The improved Li^+ mobility can be attributed to the positively charged C atoms bonded with fluorine groups. The calculations indicate stronger $TFSI^-$ binding on FGO, which facilitates Li^+ dissociation and enhances Li^+ transport. The Li||1FGO-CSE||NCM-811 cell delivers a high cathode capacity of 200 mAh g^{-1} at 25 °C, retaining 95% of its capacity after 350 cycles. While the filler-free SSE exhibits relatively low Li^+ conductivity and poor cyclability, the FGO-CSE enhances Li^+ conduction and stabilizes both the anode and cathode interfaces, thereby achieving outstanding cell performance.

1. Introduction

Solid-state Li-metal batteries (SSLMBs) have emerged as cutting-edge energy storage devices, addressing the growing demand for high energy density and high safety in various applications [1,2]. The use of a metallic Li anode, with its high theoretical capacity (3860 mAh g^{-1}) and low redox potential (−3.04 V *vs.* standard hydrogen electrode), is intended to enhance energy storage capability [3]. However,

* Corresponding author.
** Corresponding author.
*** Corresponding author.
**** Corresponding author. Department of Materials Science and Engineering, National Yang Ming Chiao Tung University, 1001 University Road, Hsinchu, 30010, Taiwan.
E-mail addresses: ccyang@mail.mcut.edu.tw (C.-C. Yang), cysu@ncu.edu.tw (C.-Y. Su), yclo@nycu.edu.tw (Y.-C. Lo), jkchang@nycu.edu.tw (J.-K. Chang).

https://doi.org/10.1016/j.compositesb.2026.113503
Received 17 November 2025; Received in revised form 31 January 2026; Accepted 6 February 2026
Available online 7 February 2026

conventional liquid-electrolyte Li-metal batteries often face challenges such as unstable solid electrolyte interphase (SEI) and Li dendrite formation, leading to poor cell cyclability and serious safety concerns [4,5]. In response, solid-state electrolytes (SSEs) have attracted increasing attention for their potential to overcome the above limitations. As a result, SSLMBs have emerged as a promising solution, offering high charge-discharge performance and enhanced reliability [6,7]. This is particularly important given the growing demand for electric vehicles and grid-scale energy management.

Generally, SSEs can be categorized as solid polymer electrolytes (SPEs), inorganic ceramic electrolytes (ICEs), and composite solid electrolytes (CSEs). SPEs, comprising a polymer matrix and lithium salts, offer flexibility, great processability, and good interfacial contact with electrodes [8]. However, they usually suffer from drawbacks including low ionic conductivity ($\sim 10^{-5}$ S cm^{-1}), limited thermal and electrochemical stability, and inadequate suppression of lithium dendrite growth [9]. In contrast, ICEs have superior ionic conductivity and high mechanical strength but exhibit insufficient interfacial connections with electrodes [10,11]. CSEs, constructed by combining SPEs and ICEs, blend the advantages of both, where the polymer phase provides flexibility, plasticity, and wettability, and the ceramic filler enhances Li^+ conduction and mechanical strength, suppressing Li dendrite propagation [12,13]. In addition, the filler particles tend to reduce crystallinity of the polymer phase, enlarging the amorphous region and creating effective pathways for Li^+ transport [14,15]. Employing a suitable filler material to enhance Li^+ conductivity and interfacial stability of the CSE is vital for the development of high-performance SSLMBs. This work addresses this pressing necessity.

Inorganic fillers in CSEs are generally classified into active and inert types according to their Li^+-conducting properties [16]. Active fillers are Li^+ conductors, such as LISICON-type, NASICON-type, perovskite-type, and garnet-type materials [14,15]. However, factors such as Li metal incompatibility (e.g., $Li_{3x}La_{2/3-x}TiO_3$, $Li_{1+x}Al_xTi_{2-x}(PO_4)_3$), high cost, limited electrochemical stability windows, and sensitivity to air and moisture (e.g., $Li_7La_3Zr_2O_{12}$) inhibit their practical application to some extent [17]. Inert fillers include oxides (e.g., SiO_2, Al_2O_3, and ZrO_2), carbon-based materials, metal-organic frameworks (MOFs), and other materials [17–19]. These inert fillers boost the CSE conductivity by reducing the polymer matrix crystallinity. Besides, they enhance Li^+ transport by forming space charge regions near their surfaces, which act as fast conduction pathways for Li^+ ions [20,21]. In addition, they can improve the CSE mechanical strength and promote the interfacial robustness [22]. Of particular importance, these fillers are usually air-stable and cost-effective, rendering them attractive for scalable SSLMBs [23].

In recent developments, certain attention has been directed toward the use of two-dimensional (2D) carbon materials as inert fillers in CSEs, owing to their environmental friendliness, high stability, and mechanical resilience [24–27]. Their two-dimensional structure establishes a continuous pathway for rapid Li^+ transport along the interface with the polymer matrix [18,21]. However, the sp^2 carbon networks impart inherent electronic conductivity, which may potentially induce cell short-circuiting and thus raise reliability concerns [26,28]. Fortunately, these materials can be engineered to show insulating behavior by disrupting the sp^2 carbon-carbon bonds through heteroatom functionalization [29]. This functionalization involves the introduction of epoxy, hydroxyl, carboxyl, and other groups onto 2D graphene sheets [29,30]. Li et al. incorporated graphene oxide (GO) into polyacrylonitrile-based SPE, achieving enhanced ionic conductivity (4.0×10^{-4} S cm^{-1}) at 30 °C due to the oxygen-functional groups, which reduce SPE polarity and improve Li salt dissociation [31]. Similarly, Wen et al. used GO into polyethylene oxide (PEO)-based SPEs, boosting the ionic conductivity (1.54×10^{-5} S cm^{-1}) and electrochemical stability, as GO suppressed PEO crystallinity and reinforced the SPE [32]. Zhang et al. coated poly (propylene carbonate) (PPC) with GO to enhance SSE/Li interface stability. Upon contact with Li metal, the GO was transformed to a reduced graphene oxide (RGO) layer, which suppressed Li dendrite growth and increased ionic conductivity to 2.22×10^{-4} S cm^{-1} at room temperature [33]. Lee et al. employed poly(ethylene glycol)-grafted GO (PGO) in a polymer matrix to achieve an ionic conductivity of 2.1×10^{-4} S cm^{-1} at 30 °C, attributed to Lewis acid–base interactions between PGO and $LiClO_4$ salt [34]. Wu et al. introduced lithiated polydopamine-modified GO nanosheets into PEO, where long-range conduction pathways with locally concentrated Li^+ form at the interfaces, yielding an enhanced CSE conductivity of 3.4×10^{-5} S cm^{-1} at 30 °C, ten times higher than that of the plain PEO electrolyte [35]. Zhu et al. and Zhang et al. modified GO with 1-(3-aminopropyl)-3-methylimidazolium bromide ionic liquid and oxyethyl-containing poly(ionic liquid), respectively [36,37]. When incorporated with PEO, the resulting CSEs exhibited ionic conductivities of 1.8×10^{-5} S cm^{-1} at 25 °C and 1.01×10^{-4} S cm^{-1} at 40 °C, respectively. Although the 2D carbon fillers have shown some promise, the ionic conductivity of the obtained CSEs remains suboptimal; thus, further investigation and improvement are required. Notably, most previous studies employed GO-based fillers in CSEs. The influence of other heteroatoms or functional groups of graphene sheets on the interactions with the polymer matrix and the consequent CSE performance has not been fully examined. Moreover, existing studies lack detailed atomic-level approaches to elucidate the fundamental mechanisms underlying the enhancement of Li^+ transport properties. This study thus aims to investigate these issues.

In the present work, three types of 2D functionalized graphene, namely RGO, GO, and fluorinated graphene oxide (FGO), are incorporated as fillers in the poly(vinylidene fluoride-co-hexafluoropropylene) (PVDF-HFP)/PPC polymer matrix with lithium bis(trifluoromethane) sulfonamide (LiTFSI) salt. For the first time, the effects of these 2D fillers on the material and electrochemical properties of CSE layers, including morphology, flexibility, thermal stability, crystallinity, ionic conductivity, Li^+ transference number (t_{Li}^+), and electrochemical stability window, are systematically studied. To enable a fair comparison among the different fillers, the filler content is initially fixed at 0.5 wt%, a concentration commonly reported to be optimal for polymer composite electrolytes [38–41]. At this loading, excessive filler–filler interactions and aggregation-induced obstruction of Li^+ transport are minimized, allowing the influence of filler surface chemistry on the electrolyte properties to be more clearly isolated [14–16,18]. Density functional theory (DFT) calculations are conducted to elucidate the Li^+ transport properties in CSE layers containing different graphene fillers. The solid-state Li/$LiNi_{0.8}Co_{0.1}Mn_{0.1}O_2$ (NCM-811) cells are assembled using various SSEs and tested at 25 °C. Although many previous studies have employed elevated temperatures to enhance the performance of SSLMBs, this work aims to achieve high capacities at room temperature. After identifying FGO as the most effective filler, the effect of FGO concentration is further examined in an effort to maximize battery performance. For a Li||1FGO-CSE||NCM-811 cell, a reversible capacity of 200 mAh g^{-1} is achieved for NCM-811 at 25 °C. The capacity retention after 350 charge-discharge cycles is as high as 95%. These superior properties are attributed to FGO enhancing the CSE ionic conductivity to 9.4×10^{-4} S cm^{-1} at 25 °C and promoting the formation of stable interfaces at both the anode and cathode sides. The CSE containing FGO fillers demonstrates substantial potential for practical applications in SSLMBs. This study elucidates the unique roles of FGO in SSLMBs and provides important insights for the development of high-performance batteries.

2. Results and discussion

Fig. 1a–c shows transmission electron microscopy (TEM) images of the RGO, GO, and FGO samples, whose synthesis procedures are provided in the Supporting Information. All samples exhibit high electron transparency, indicating that these 2D carbon fillers consist of only a few atomic layers. In addition, these samples exhibit many characteristic wrinkles, which are typical features of the graphene materials prepared

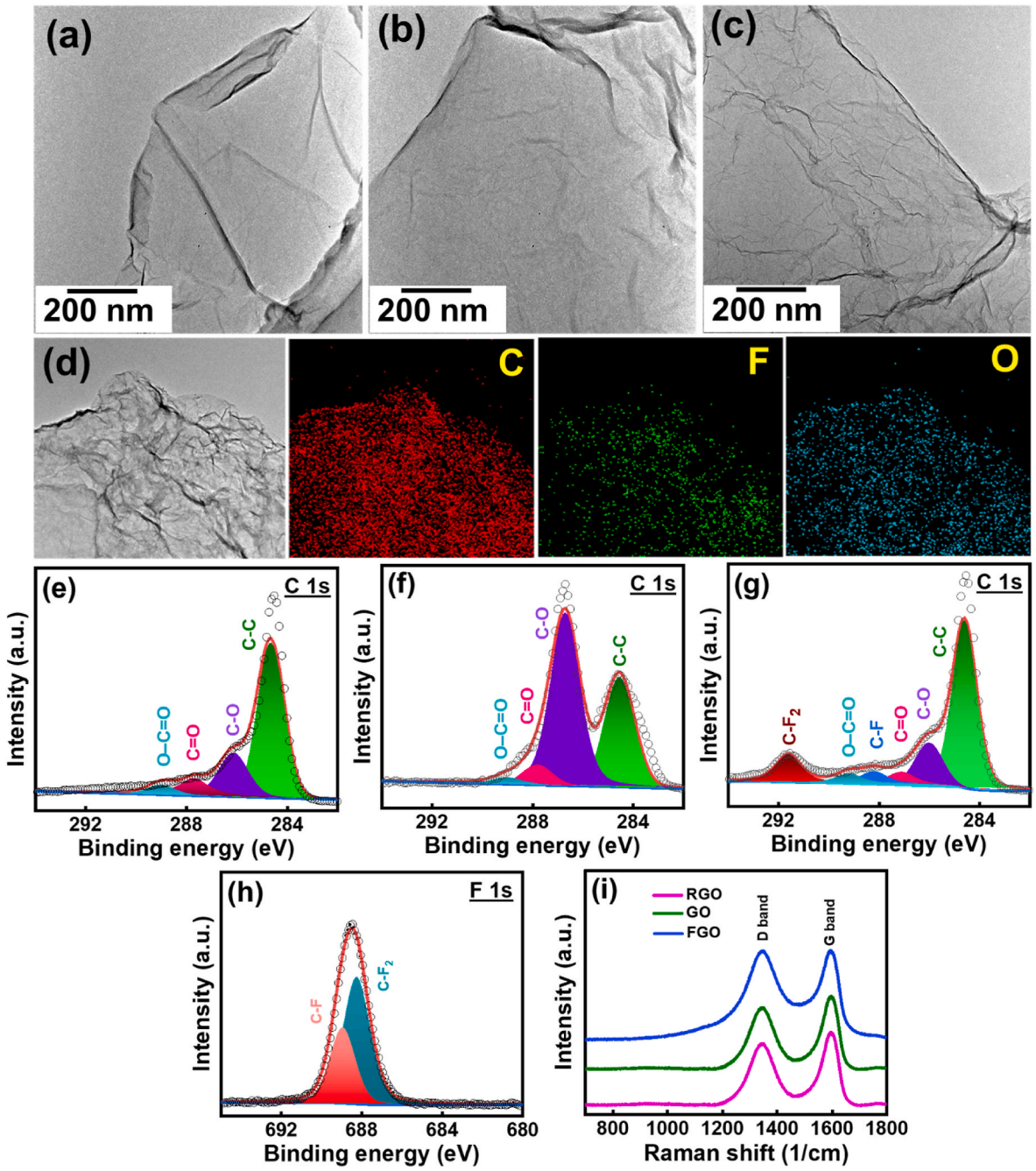

Fig. 1. TEM images of (a) RGO, (b) GO, and (c) FGO fillers. (d) EDS elemental mapping results of FGO. High-resolution XPS C 1s spectra of (e) RGO, (f) GO, and (g) FGO. (h) XPS F 1s spectrum of FGO. (i) Raman spectra of RGO, GO, and FGO fillers.

via chemical/electrochemical exfoliation [42]. The wrinkles are associated with the presence of sp^3 hybridized carbons, which are associated with the presence of various functional groups and structural defects in the materials [43]. Fig. 1d shows the scanning TEM energy-dispersive X-ray spectroscopy (EDS) mapping results of the FGO sample (the data of the RGO and GO samples are shown in Fig. S1). As shown, fluorine, along with carbon and oxygen, is uniformly distributed throughout the FGO sample. Atomic force microscopy (Fig. S2) confirms that the FGO nanosheets exhibit micrometer-scale lateral dimensions and a thickness of approximately 5.5 nm. X-ray photoelectron spectroscopy (XPS) was employed to characterize the chemical composition of the samples. The high-resolution XPS C 1s profiles of RGO, GO, and FGO are shown in Fig. 1e–g. The deconvoluted spectra reveal peaks at 284.6, 286, 287.1, and 288.8 eV, corresponding to C–C, C–O, C═O, and O–C═O, respectively [44]. RGO was synthesized from GO via chemical reduction, leading to a notable decrease in the oxygen-containing functional group concentration. In addition to these bonds, the deconvoluted spectrum of FGO (Fig. 1g) shows C/F bonding states, including C–F at 288.2 eV and C–F_2 at 291.6 eV. The F 1s spectrum of FGO also reveals the formation of C–F and C–F_2 bonds (Fig. 1h) [45]. Table S1 shows the atomic percentage of constituent elements in RGO, GO, and FGO. The F content in the last sample is 17.8%, confirming an effective fluorination of the graphene material. No attempt was made to optimize the fluorination degree in this study. However, at this fluorination level, FGO is electronically insulating, which prevents electronic conduction of the CSE [46–48]. Although a higher degree of fluorination could further strengthen interactions between FGO and the polymer matrix, it may also excessively disrupt the sp^2 conjugation of the graphene sheets,

leading to deterioration of their physicochemical properties. Therefore, systematic optimization of the fluorination degree requires further investigation. Raman spectroscopy was employed to investigate the carbon bonding characteristics of various samples. Fig. 1i shows the Raman data of RGO, GO, and FGO samples. Two characteristic bands are observed, including the *D* band (at ~1350 cm^{-1}) associated with imperfect sp^2 carbon bonding and the *G* band (at ~1585 cm^{-1}) related to in-plane vibration of a well-ordered graphitic lattice [49]. The *D*-to-*G* band intensity ratio (I_D/I_G) was calculated to assess the degree of structural defect. The I_D/I_G values for RGO, GO, and FGO are 0.846, 0.892, and 0.998, respectively. GO shows more defects than RGO due to the higher concentration of oxygen-containing functional groups that disrupt the carbon sp^2 network. Further fluorination introduces new covalent C/F bonds, which render structural disorder and consequently increase the I_D/I_G ratio.

The preparation procedures of the SPE (without fillers) and various CSE layers are described in the Supporting Information and Scheme 1. The carbon filler content was fixed at 0.5 wt% unless otherwise specified. Fig. 2a and b shows the scanning electron microscopy (SEM) plan-view images of SPE and FGO-CSE (those for RGO-CSE and GO-CSE are presented in Fig. S3a and b). The pristine SPE exhibits a relatively rough morphology with the presence of micropores, which is typical for PVDF-based SSEs [27]. Upon incorporating the carbon fillers, the polymer matrices become more interconnected. As shown in the insets of Fig. 2a and b, the white color of the pristine SPE layer changes to a dark grey color due to the addition of FGO. Fig. 2c illustrates the high flexibility of the FGO-CSE layer. Fig. 2d and e presents the SEM cross-sectional images of SPE and FGO-CSE, while those of RGO-CSE and GO-CSE are shown in Fig. S3c and d. The pristine SPE exhibits a less uniform morphology, with large voids present within the electrolyte layer. In contrast, all the CSEs show finer and more homogeneous structures, suggesting that the fillers are well dispersed and alter the microstructure of the PVDF-HFP/PPC polymer. The cross-sectional examination results indicate that the thicknesses of the SPE and CSEs are all approximately 75 μm.

The thermal stability of SSE is a crucial factor in determining the battery reliability and safety. Fig. 2f shows the thermogravimetric curves of the SPE and FGO-CSE samples. The data for a conventional organic electrolyte (1 M $LiPF_6$ in ethylene carbonate/diethyl carbonate) are included for comparison, which exhibit a significant weight loss of ~40% before 100 °C. This is associated with vigorous evaporation of the carbonate solvent and decomposition of $LiPF_6$ into LiF and PF_5 [50]. In contrast, the SPE and FGO-CSE samples exhibit improved thermal stability. The slight weight loss observed below 100 °C is attributed to the removal of adsorbed moisture. According to prior reports [51,52], residual DMF typically evaporates in the temperature range of 140–200 °C. However, no discernible mass loss is observed in this region in the thermogravimetric profiles, indicating that the residual DMF content in the electrolyte layers is negligible. The small step at ~210 °C is attributed to the deterioration of PPC [53]. The major thermal degradation occurred above ~320 °C, the weight change is mainly related to the decomposition of PVDF-HFP and LiTFSI [54]. Since the FGO filler accounts for only 0.5 wt% in the CSE, it does not substantially alter the thermal behavior of the electrolyte layer.

Differential scanning calorimetry (DSC) was conducted to determine the melting temperature (T_m), which reflects the degree of crystallinity [55], of the polymer matrices containing various fillers. As shown in Fig. 2g, the T_m values of the SPE, RGO-CSE, GO-CSE, and FGO-CSE samples are approximately 150 °C, 146 °C, 144 °C, 140 °C, respectively. The results indicate that incorporation of the carbon fillers reduces the crystallinity and increases the amorphous fraction of the polymer phase, which is favorable for Li^+ transport [31,32,35]. The fact that FGO reduces the crystallinity to the greatest extent suggests that the highly electronegative fluorine groups enhance interfacial interactions, effectively disrupting the ordered stacking of the polymer chains.

Ionic conductivity is a key property of SSEs, exerting a significant influence on overall battery performance. Symmetrical cells using Al blocking electrodes were used to evaluate the Li^+ conductivity of various electrolyte layers. The EIS Nyquist plots obtained at 25 °C are shown in Fig. 2h and can be fitted using the equivalent circuit illustrated in the inset, where *R* and *Q* represent the electrolyte resistance and constant phase element, respectively [56]. The intercepts with the real axis correspond to the electrolyte resistances [57]. The calculated ionic conductivity values of the SPE, RGO-CSE, GO-CSE, and FGO-CSE are 6.0 × 10^{-4}, 7.0 × 10^{-4}, 7.8 × 10^{-4}, and 8.8 × 10^{-4} S cm^{-1}, respectively. The fillers decrease the crystallinity of the polymer, which is beneficial for enhancing ionic conductivity [18–21]. The t_{Li}^+ value is another important parameter for evaluating Li^+ transport capability in the electrolyte. The t_{Li}^+ values were calculated using the Bruce-Vincent method [58]; the details are provided in the Supporting Information. Fig. 2i shows the chronoamperometric curve and EIS data measured before and after the polarization of the Li||FGO-CSE||Li cell (the data for other cells are shown in Fig. S4). The t_{Li}^+ of the SPE is 0.29, whereas with the RGO, GO and FGO fillers the values increase to 0.34, 0.48, and 0.60, respectively. The results indicate that FGO effectively enhances both the ionic conductivity and t_{Li}^+ of the CSE layer (Fig. 2j). Although the FGO-CSE exhibits a significantly higher t_{Li}^+, the increase in total ionic conductivity is comparatively moderate. The total ionic conductivity reflects the combined contributions of both cationic and anionic charge carriers. In the filler-free SPE, a large fraction of the conductivity arises from the highly mobile $TFSI^-$ anions. In contrast, in the FGO-CSE, strong interactions between FGO and $TFSI^-$ suppress anion mobility, thereby increasing the t_{Li}^+ value. However, the reduction in the anionic contribution limits the overall gain in total conductivity. The underlying mechanism is further elucidated by DFT calculations, which will be discussed later. Temperature-dependent ionic conductivity measurements (Fig. S5) yield activation energies of 0.28 eV for the SPE and 0.20 eV for the FGO-CSE, indicating facilitated Li^+ transport in the presence of FGO.

The electrochemical stability windows (ESWs) of various SSEs were

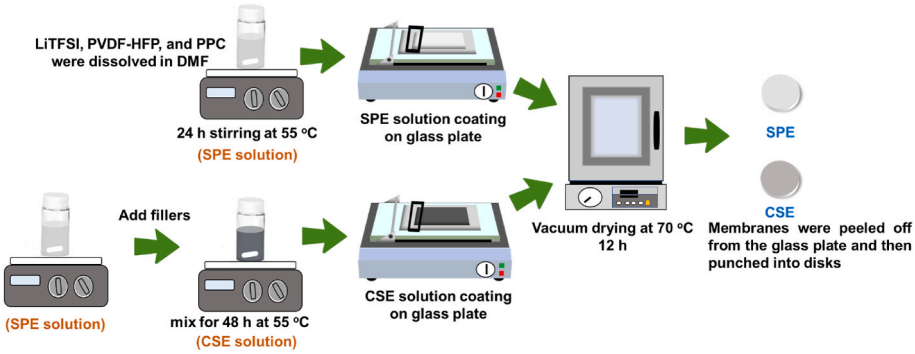

Scheme 1. Fabrication procedures of SPE (without fillers) and CSE layers.

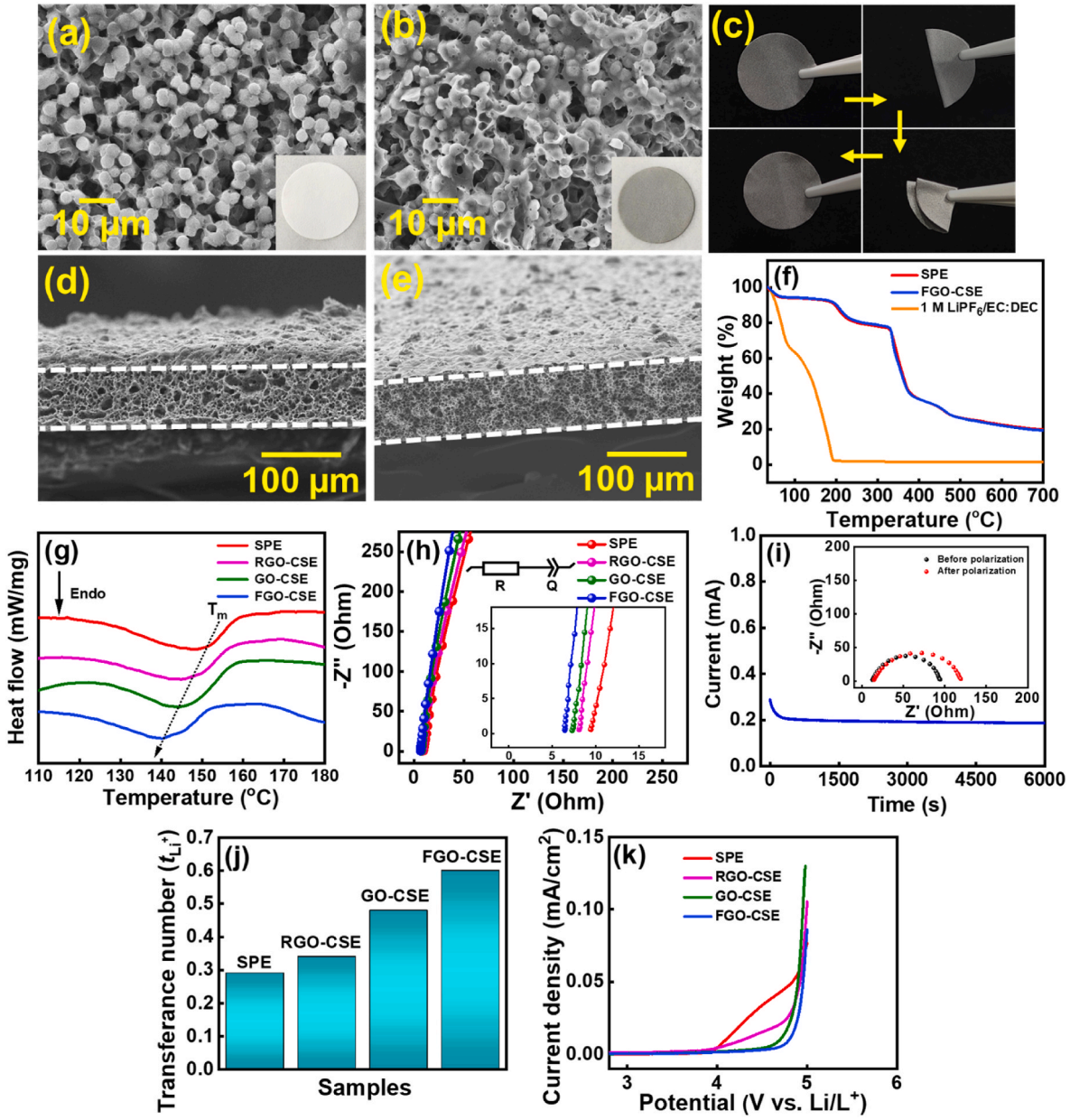

Fig. 2. SEM plan-view images of (a) SPE and (b) FGO-CSE. The figure insets show the appearances of electrolyte membranes. (c) Flexibility test results of FGO-CSE. SEM cross-sectional images of (d) SPE and (e) FGO-CSE. (f) TGA data of various electrolytes. (g) DSC and (h) EIS conductivity measurement data of various SSEs. (i) Chronoamperometric curve and EIS data measured before and after 10 mV polarization of Li||FGO-CSE||Li cell. (j) The t_{Li}^{+} values and (k) LSV data of various SSEs.

evaluated via linear sweep voltammetry (LSV). Fig. 2k shows the obtained LSV data recorded at the Al electrodes. The SPE began to decompose at ~4.0 V vs. Li/Li^+, which is in line with the literature data [59,60]. However, the ESW can be extended through the incorporation of carbon fillers. Notably, the FGO-CSE demonstrates the largest ESW, reaching ~4.8 V vs. Li/Li^+, which is highly promising for high-voltage Li batteries. The strong electronegativity of the fluorine groups exerts a pronounced inductive effect on the surrounding carbon framework of the FGO, which in turn withdraws electron density from the interacting polymer chains. This electron-withdrawing interaction effectively lowers the highest occupied molecular orbital (HOMO) energy level of the polymer phase [61]. The reduced HOMO energy increases the energy required for electron removal (i.e., oxidation), thus raising the oxidation onset potential of the FGO-CSE. Additionally, the fluorine groups facilitate the formation of a robust electrode/electrolyte interphase, which suppresses unfavorable side reactions [62,63]. It was also reported that the fluoride-rich interphase can scavenge reactive radicals, thereby mitigating electrolyte decomposition at high voltage [63–65]. As a result of these combined effects, FGO exhibits superior performance compared to GO and RGO in extending the ESW.

To investigate the effects of different graphene fillers in SSEs and to gain atomistic insights into their functions, DFT calculations were employed. The calculation details are described in the Supporting Information. Based on the XPS data, which revealed the types of various functional groups, we constructed various types of 9 × 9 graphene supercells: one with lower hydroxyl and epoxide contents representing RGO, and another enriched with these groups representing GO. For FGO, we introduced a carbon vacancy in the RGO model and incorporated F atoms. The model containing both C–F and C–F_2 bonds is denoted FGO-HF, whereas the model with a lower degree of fluorination, containing only a C–F_2 bond, is denoted FGO-LF. The structural details of the RGO, GO, FGO-LF, and FGO-HF are shown in Fig. 3a–d. The interaction

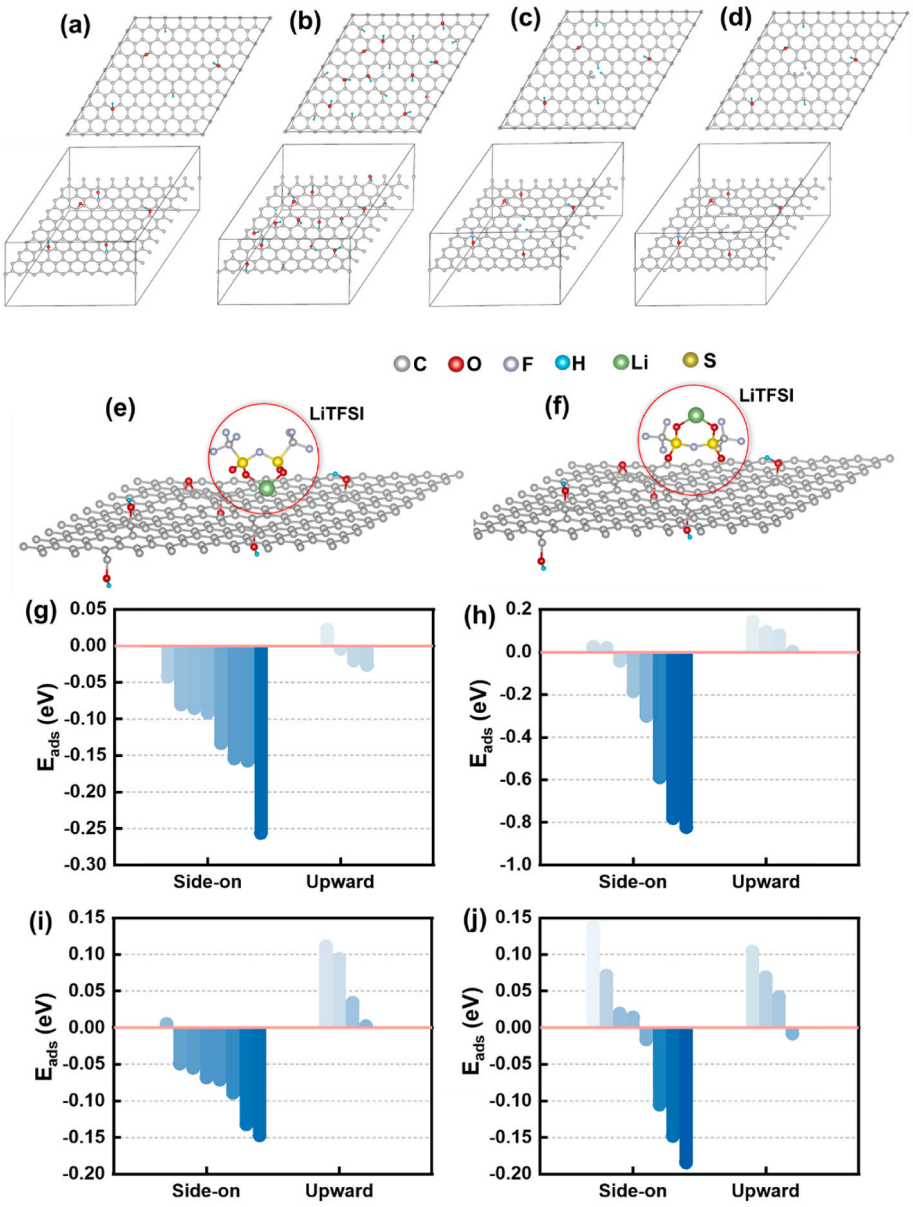

Fig. 3. Structural models of (a) RGO, (b) GO, (c) FGO-LF, and (d) FGO-HF proposed based on XPS and Raman analyses. Two contact configurations between LiTFSI and graphene substrate: (e) side-on contact and (f) upward contact. Adsorption energy of LiTFSI on (g) RGO, (h) GO, (i) FGO-LF, and (j) FGO-HF models with side-on and upward contact configurations.

between LiTFSI and various graphene models as well as the interaction between Li^+ ions and the surrounding species are elucidated by the adsorption energy (E_{ads}) and binding energy (E_b), respectively. First, we examined two contact configurations of LiTFSI adsorbed on the graphene substrate, referred to as "side-on" and "upward," as shown in Fig. 3e–f. In total, 12 adsorption sites with two different contact configurations were examined; the corresponding E_{ads} values are shown in Fig. 3g–j. Across the four substrates, the E_{ads} data indicate that the side-on contact is energetically more favorable. Of note, the E_{ads} values on FGO-LF and FGO-HF are clearly lower than those on the other substrates, implying better LiTFSI mobility on FGO.

The binding strength between Li^+ ions and the surrounding species, including $TFSI^-$ anions and functionalized graphene sheets, was further evaluated. Fig. 4a shows the E_b values of Li^+ ions in the side-on-contacted LiTFSI on various graphene substrates. The binding strength of Li^+ ions on FGO-LF (−3.945 to −4.210 eV) and FGO-HF (−3.913 to −4.227 eV) is weaker than on RGO and GO, indicating that Li^+ transport is easier in the former two models. These results are consistent with the Li^+ conductivity trend: FGO-CSE > GO-CSE > RGO-CSE. The E_b values sampled on GO display a wide distribution. It is noteworthy that three exceptionally strong E_b values (−4.695, −4.737, and −4.965 eV) are observed. This high binding is attributed to the bond formation between Li^+ ions and hydroxyl groups (see Fig. 4b). This phenomenon is explained in the following section. Except for these particular cases, the binding strengths of Li^+ ions at other adsorption sites are relatively weaker. Thus, the GO model, compared with RGO, provides more weak binding sites for Li^+ ions, thereby facilitating Li^+ transport. To examine Li^+ mobility from a kinetic perspective, we calculated the mean squared displacement (MSD) using *ab initio* molecular dynamics (AIMD) simulations. Fig. 4c–f shows the MSD of Li^+ along three directions on the four functionalized graphene materials. As compared in Fig. 4g, the MSD data follow the trend FGO-HF > FGO-LF > GO > RGO. These results indicate that Li^+ ions exhibit greater mobility on the FGO surface.

To investigate the Coulomb interactions of Li^+ ions with the RGO,

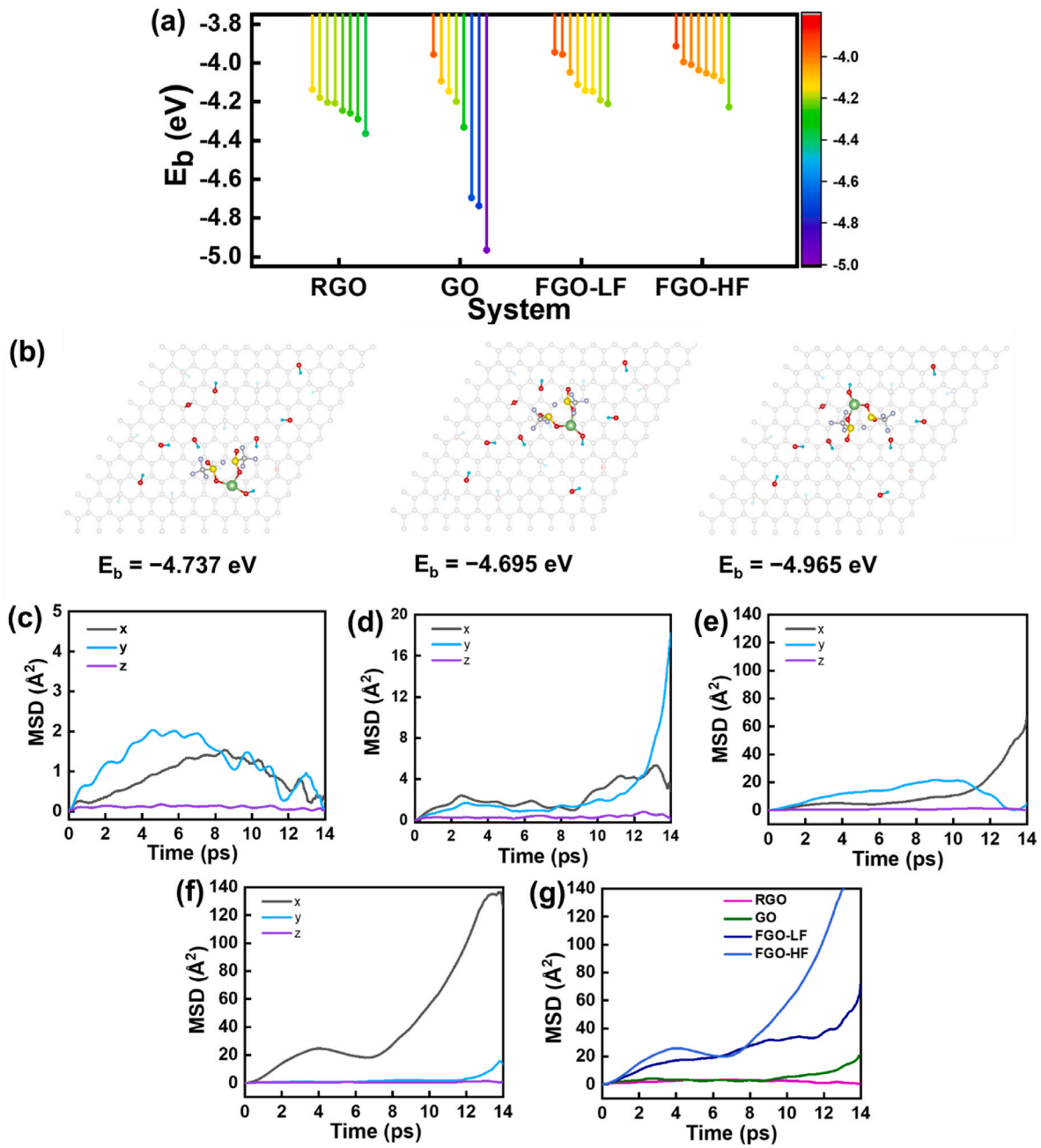

Fig. 4. (a) Binding energy of Li^+ on four types of functionalized graphene models. (b) Three different geometric configurations of LiTFSI on GO and the corresponding binding energy of the Li^+ ion. Three directional components of MSD for Li^+ ion migration on (c) RGO, (d) GO, (e) FGO-LF, and (f) FGO-HF models. (g) Overall MSD of Li^+ ion on various substrates.

GO, FGO-LF, and FGO-HF models, Bader charge analysis was performed. Fig. 5a–d depicts the density of Bader charge difference (DOB) profiles for each element within the functionalized graphene materials. As expected, the H atoms carry positive charges, whereas the O and F atoms carry negative charges. Although F generally has a higher electronegativity than O (3.98 vs. 3.44), the F atoms in the FGO-LF and FGO-HF models (Fig. 5c and d) carry less negative charge than the O atoms. This can be attributed to the intrinsic valence preferences of the elements, with O favoring a −2 oxidation state and F favoring a −1 oxidation state. Because the O atoms carry the most negative charge, Li^+ ions are strongly attracted to them, hindering Li^+ transport. In addition, the C atoms in the RGO model exhibit minimal charge transfer. In comparison, the GO model contains more positively charged C atoms than the RGO model. Most importantly, in the FGO-LF and FGO-HF models, the C atoms near the structural vacancies exhibit pronounced positive charges (indicated by the arrows in the figures). As a result, the average electropositivity of C atoms follows the trend FGO-HF > FGO-LF > GO > RGO. The results indicate that this electropositivity can be controlled by the type and configuration of the functional groups. It affects the binding strength with Li^+ ions, explaining the differences in the Li^+ transport properties.

Fig. 5e–h presents the potential energy landscape (PEL) profiles and the corresponding 2D projections based on the Bader charge difference of C atoms for the four graphene models. The blue regions in the PEL plots represent positively charged regions that can attract $TFSI^-$ anions. The attraction of $TFSI^-$ anions subsequently facilitates Li salt dissociation and increases t_{Li}^+ [15,16]. As shown in Fig. 5e, the PEL plot of RGO exhibits a relatively flat contour with fewer PE valleys (denoted as “V” in

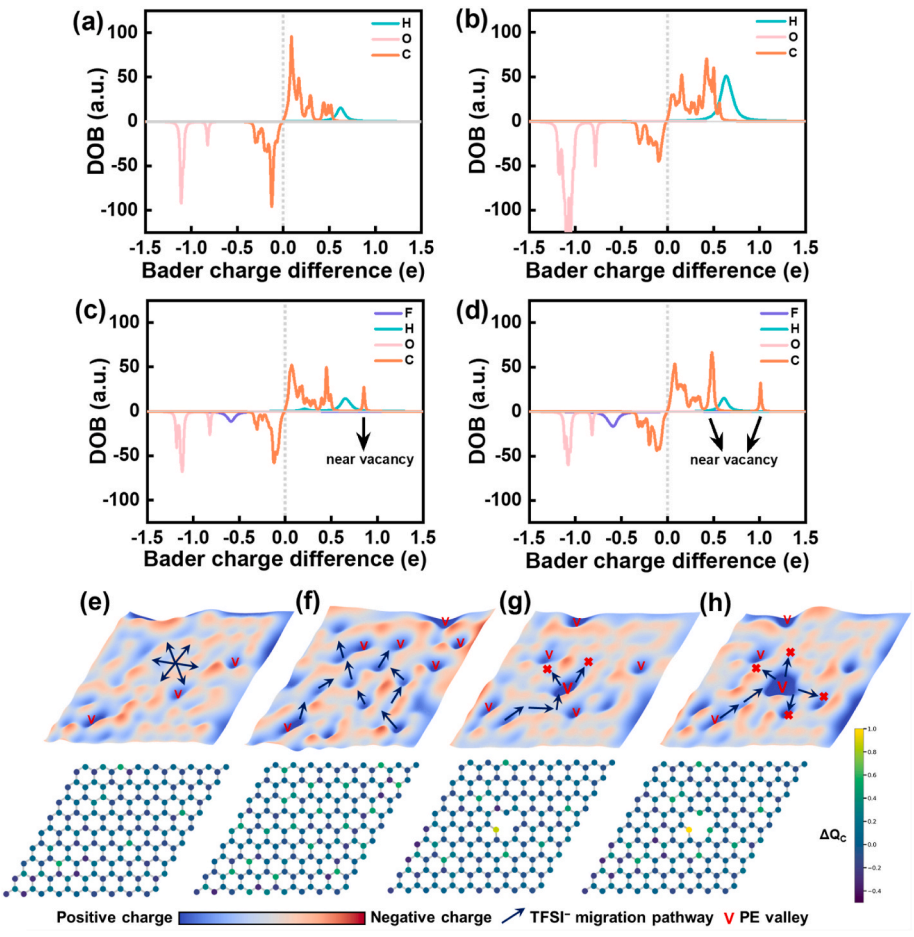

Fig. 5. DOB profiles for each element within (a) RGO, (b) GO, (c) FGO-LF, and (d) FGO-HF models. PEL profiles and corresponding 2D projections based on Bader charge difference of C atoms for (e) RGO, (f) GO, (g) FGO-LF, and (h) FGO-HF models.

the figure). This facilitates isotropic migration of $TFSI^-$ anions while limiting the formation of free Li^+ ions. As for the GO model (Fig. 5f), the multiple PE valleys trap $TFSI^-$ anions, thereby promoting the release of free Li^+ ions. As shown, once the $TFSI^-$ anions overcome the potential barrier, they migrate along specific pathways rather than moving isotropically. Hence, the transport of free Li^+ is enhanced compared with that on RGO. In the FGO-LF and FGO-HF models, deep PE valleys form around the vacancy sites (Fig. 5g and h). This can be attributed to the defective carbon configuration and the high electronegativity of F atoms. In these deep PE valleys, $TFSI^-$ anions struggle to overcome the potential barriers, resulting in strong trapping. Notably, the F atom content strongly affects both the depth and dimension of the PE valleys, as shown in the PEL profiles and corresponding 2D projections of the two FGO models. The unique structure of FGO-HF accounts for the significant improvements observed in both Li^+ conductivity and t_{Li}^+ values.

The binding strength of $TFSI^-$ anions on various graphene samples was also evaluated. As shown in Fig. S6, the binding strength on FGO-LF (ranging from −1.433 to −1.615 eV) and FGO-HF (ranging from −1.407 to −1.650 eV) is clearly stronger than that on GO and RGO. These data align with the Bader charge analysis results of C atoms (Fig. 5a–d), elucidating the interactions between $TFSI^-$ and functionalized graphene surfaces.

The DFT and AIMD simulations in this work primarily focus on Li^+ transport at interfaces involving graphene-based fillers and LiTFSI salt. The challenges associated with explicitly incorporating the polymer phase are discussed in the Supporting Information. Despite this simplified model, the MSD profiles indicate that Li^+ migration occurs preferentially parallel to the carbon surface. The simulations further reveal that Li^+ mobility is strongly governed by charge redistribution within the carbon framework. These insights may guide the future design of functional fillers for improving CSE performance.

The interfacial compatibility and long-term stability between the SSE and the lithium metal electrode are critical for SSLMB performance. To assess these interfacial properties, galvanostatic cycling tests were conducted on symmetric Li||SSE||Li cells. Fig. 6a shows the obtained data of Li||SPE||Li and Li||FGO-CSE||Li cells. The latter cell exhibits stable cycling for over 1000 h at 25 °C under a current density of 0.1 mA cm^{-2}, whereas the former cell breaks down after ~650 h. The absence of significant voltage oscillations during long-term cycling of the latter cell suggests that FGO incorporation enhances the interfacial stability. To gain insight into the Li plating/stripping behavior of the two cells, the surface morphologies of Li metal electrodes recovered from the symmetric cells were examined. As shown in Fig. 6b, the Li electrode cycled with SPE exhibits a discolored appearance and irregular lithium deposits. In contrast, the Li electrode cycled with FGO-CSE (Fig. 6c) remains clean, exhibiting a smooth and uniform morphology. This can be attributed to the ability of FGO fillers to homogenize Li^+ flux and increase the t_{Li}^+ of the SSE, thereby suppressing the inhomogeneous evolution of the lithium surface. Fig. S7 shows the XPS depth-profiling data of the Li electrode cycled with FGO-CSE. The surface region is enriched in carbon and oxygen, which are associated with residual electrolyte species, while the Li signal increases monotonically with depth. Notably, a broad distribution of fluorine is observed, indicating the formation of a distinct fluorine-rich SEI that contributes to the sustained interfacial stability during cycling. SEM analyses were also conducted on the SSE sides after cycling (Fig. 6d and e). The SPE layer exhibits significant

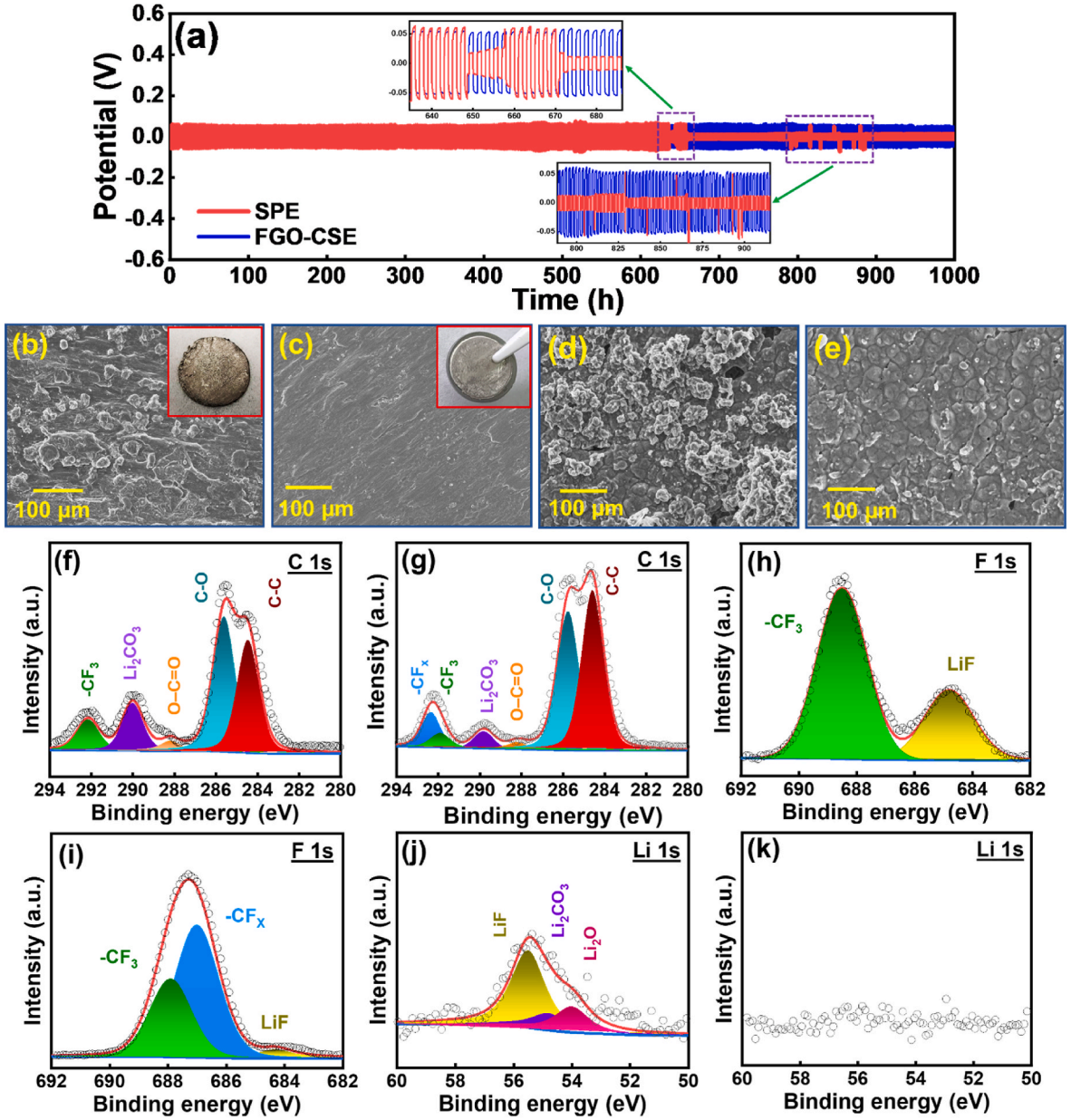

Fig. 6. (a) Galvanostatic cycling profiles of Li||SPE||Li and Li||FGO-CSE||Li cells, with charge and discharge periods of 1 h. SEM and optical images of Li electrodes cycling with (b) SPE and (c) FGO-CSE. SEM images of (d) SPE and (e) FGO-CSE after cycling. High-resolution XPS spectra of cycled samples: C 1s for (f) SPE and (g) FGO-CSE, F 1s for (h) SPE and (i) FGO-CSE, and Li 1s for (j) SPE and (k) FGO-CSE.

accumulation of byproducts and dead Li on its surface. Conversely, the surface of the FGO-CSE basically remains intact, with fewer discernible byproducts after 1000 h of cycling. To evaluate the high-rate capability of the SSEs, Li||SPE||Li and Li||FGO-CSE||Li cells were tested under progressively increasing current densities. As shown in Fig. S8, the Li||SPE||Li cell exhibits significantly higher voltage polarization across the entire current range and begins to short-circuit at 2.5 mA cm^{-2}. In contrast, the Li||FGO-CSE||Li cell demonstrates superior tolerance to high current densities, operating stably without short-circuiting up to 5 mA cm^{-2}.

XPS was employed to examine the surface chemistry of the SPE and FGO-CSE layers after cycling. Fig. 6f shows the C 1s spectrum of the cycled SPE, which exhibits relatively strong C–O and O–C═O peaks along with a significant Li_2CO_3 signal, indicating pronounced side reactions between the Li electrode and SPE. The peak at ~292.0 eV, corresponding to $–CF_3$ species, confirms substantial decomposition of the PVDF-HFP phase. These features correspond to the thick, nonuniform covering layer observed in Fig. 6d. For FGO-CSE (Fig. 6g), the peaks of C–O, O–C═O, Li_2CO_3, $–CF_3$ are markedly reduced, whereas a new peak at ~292.3 eV, attributed to $–CF_x$ species likely derived from FGO, emerges. It is postulated that this unique $–CF_x$ interface mitigates undesirable side reactions, thereby stabilizing the cycling performance shown in Fig. 6a. The F 1s spectra of the SPE (Fig. 6h) and FGO-CSE (Fig. 6i) samples fully validate the above arguments. The Li 1s spectra in Fig. 6j and k indicate that the SPE surface is enriched with LiF, Li_2CO_3, and Li_2O, whereas the FGO-CSE surface contains almost no residual Li species.

Solid-state Li/NCM-811 cells with SPE, RGO-CSE, GO-CSE, and FGO-CSE electrolytes were assembled and tested in a voltage range of 2.7–4.3 V at 25 °C. Detailed procedures for electrode fabrication and coin cell assembly are provided in the Supporting Information Fig. 7a and b shows the charge-discharge curves of SPE and FGO-CSE cells. The charge-discharge profiles of the other cells are shown in Fig. S9. As summarized in Table 1, the capacities measured at 25 mA g^{-1} are 170,

Table 1
Comparison of reversible specific capacities of NCM-811 cathodes measured at different current rates using various types of SSEs.

Current rate (mA g^{-1})	Discharge capacities (mAh g^{-1})					
	SPE	RGO-CSE	GO-CSE	FGO-CSE	1FGO-CSE	2FGO-CSE
25	170	173	180	185	200	180
50	142	146	151	163	177	158
75	120	123	127	143	158	139
100	104	107	109	130	139	122
200	64	66	70	88	99	80
300	45	49	52	64	80	57
High rate retention[a]	26 %	28 %	30 %	35 %	40 %	32 %
Capacity retention after 350 cycles	61 %	66 %	80 %	90 %	95 %	88 %

[a] a comparison between reversible capacities at 300 and 25 mA g^{-1}.

173, 180, and 185 mAh g^{-1} for the SPE, RGO-CSE, GO-CSE, and FGO-CSE cells, respectively. Fig. 7c compares the rate capabilities of the various cells. The Li||FGO-CSE||NCM-811 cell delivered capacities of 163, 143, 130, 88, and 64 mAh g^{-1} at current densities of 50, 75, 100, 200, and 300 mA g^{-1}, respectively, demonstrating superior rate capability. The capacity retention of the SPE, RGO-CSE, GO-CSE, and FGO-CSE cells at 300 mA g^{-1}, relative to their capacities at 25 mA g^{-1}, is 26%, 28%, 30%, and 35%, respectively. The superior performance of the FGO-CSE cell is attributed to the enhanced Li^+ dissociation, promoted Li^+ mobility, and high t^+_{Li}, as revealed by the DFT calculations. EIS was employed to examine the impedance characteristics of various cells after five conditioning cycles; the obtained data are shown in Fig. 7d. The equivalent circuit used to characterize the EIS spectra is shown in the figure inset. The R_e, R_{ct}, *CPE*, and *W* represent the electrolyte resistance, charge transfer resistance, interfacial constant phase element, and Warburg impedance associated with Li^+ diffusion within the electrode, respectively [66]. The R_{ct} values of the SPE, RGO-CSE, GO-CSE, and

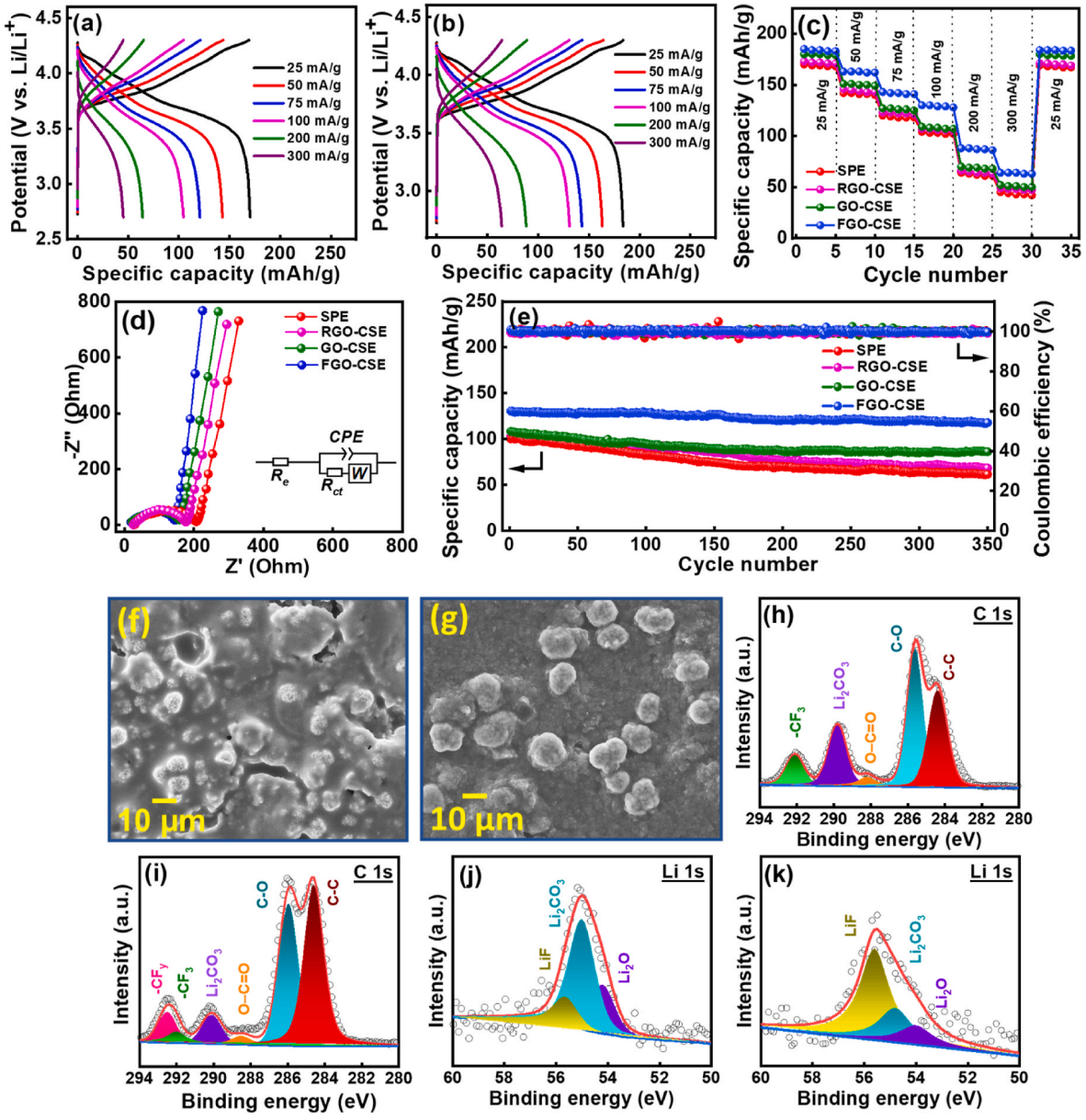

Fig. 7. Galvanostatic charge-discharge curves of (a) Li||SPE||NCM-811 and (b) Li||FGO-CSE||NCM-811 cells. (c) Comparative rate performance, (d) EIS spectra after conditioning cycles, and (e) cycling stability data (measured at 100 mA g^{-1}) of Li/NCM-811 cells with various SSEs. Postmortem SEM images of NCM-811 electrodes cycled with (f) SPE and (g) FGO-CSE. High-resolution XPS spectra of NCM-811 electrodes cycled with (h,j) SPE and (i,k) FGO-CSE.

FGO-CSE cells are 176, 152, 137, and 115 Ω, respectively. The improved charge transfer property of the Li||FGO-CSE||NCM-811 cell explains its superior high-rate performance. The cyclic voltammetry (Fig. S10) and dQ/dV data (Fig. S11) of the Li||SPE||NCM-811 and Li||FGO-CSE||NCM-811 cells indicate that, although the redox features are not altered, the latter cell exhibits clearly improved kinetics and reduced internal resistance, consistent with the galvanostatic charge-discharge behavior.

Fig. 7e shows the cycling performance of solid-state cells with various SSEs evaluated at 100 mA g^{-1}. After 350 cycles, the capacity retention of the SPE, RGO-CSE, GO-CSE, and FGO-CSE cells was 61%, 66%, 80%, and 90%, respectively. Clearly, the introduction of an appropriate filler material into the polymer electrolyte can improve the cycling stability of the Li/NCM-811 cell. The microstructures of the NCM-811 cathodes after 350 charge-discharge cycles were examined to investigate the causes of performance degradation. The SEM image (Fig. 7f) shows that the cathode cycled with SPE has lost its mechanical integrity and displays pronounced surface cracks. In contrast, with FGO-CSE (Fig. 7g), the cathode remains undamaged and is coated with a uniform cathode-electrolyte interphase (CEI) layer. The SEM images of the anodes after cycling are shown in Fig. S12. The Li electrode from the Li||SPE||NCM-811 cell exhibits a rough and heterogeneous surface with pronounced morphological irregularities. In contrast, the Li electrode recovered from the Li||FGO-CSE||NCM-811 cell displays a comparatively smooth and uniform surface. The electrode surface chemistry was examined using XPS. The C 1s spectra of the NCM-811 cathodes cycled with SPE and FGO-CSE are shown in Fig. 7h and i. For the SPE-cycled electrode, the pronounced C–O, O–C═O, Li_2CO_3, and $–CF_3$ peaks indicate severe decomposition of the SPE layer. The substantial presence of Li_2CO_3 is undesirable due to its poor ionic and electronic conductivity [67,68]. Its brittle nature is detrimental to the mechanical stability of the CEI [69,70]. In comparison, the electrode cycled with FGO-CSE exhibits significantly weaker signals of these decomposition products. Notably, a new peak at ~292.6 eV, attributable to $–CF_y$ species, appears. This is likely due to the fluorine in FGO reacting at the electrode/electrolyte interface under high potential. The resulting fluorine-rich CEI is protective and effectively suppresses the unwanted interfacial side reactions. Fig. 7j and k shows the Li 1s spectra of the same electrodes. The SPE-cycled sample exhibits a dominant Li_2CO_3 peak, consistent with the C 1s data (Fig. 7h), whereas the FGO-CSE-cycled sample is enriched with LiF species. The LiF-rich CEI offers excellent passivation and mechanical strength [71–73], resulting in the long cycling longevity of the Li||FGO-CSE||NCM-811 cell (Fig. 7e). In addition, the concentrations of metal species (Ni, Co, and Mn) on the NCM-811 electrode cycled with SPE are clearly lower than those on the electrode cycled with FGO-CSE, as shown in Table S2. These data suggest that the CEI layer on the latter electrode after cycling is thinner than that on the former electrode. Fig. S13 shows the depth-resolved time-of-flight secondary ion mass spectrometry data of the cycled Li anode and NMC-811 cathode obtained from Li||FGO-CSE||NCM-811 cell. The results reveal abundant fluorine-containing species, including Li^+, F^-, CF^-, CF_2^-, and CF_3^- at both electrodes. These species are present not only near the surface but also persist to a certain depth, confirming the formation of LiF and CF_x/CF_y interfacial components, consistent with the XPS analysis.

Fig. 8a illustrates the degradation mechanism of charge-discharge performance in the Li||SPE||NCM-811 cell. An unstable SEI leads to continuous formation of rough and dendritic lithium on the anode. At the cathode side, the unfavorable CEI, dominated by C–O and Li_2CO_3 species, fails to stabilize the NCM-811/SPE interface and hinders effective Li^+ transport. Consequently, the cell experiences significant deterioration upon cycling. In contrast, as illustrated in Fig. 8b, the FGO-CSE enhances Li^+ conduction, suppresses electrolyte anion mobility, and homogenizes Li^+ flux, thereby enabling smooth Li deposition/stripping. In addition, the FGO-CSE facilitates the formation of LiF- and CF_x/CF_y-enriched interfaces at both the anode and cathode sides. These fluorine-rich SEI and CEI layers effectively suppress the decomposition side reactions, thereby protecting the Li and NCM-811 electrodes and enhancing their redox reversibility. These features contribute to the superior electrochemical performance and cycle life of the Li||FGO-CSE||NCM-811 cell.

Since the FGO-CSE exhibits the most promising properties, we further investigate the effects of FGO filler concentration on the performance of Li/NCM-811 cells. Higher FGO amounts (1 and 2 wt%) are incorporated into the CSE, and the resulting samples are denoted as 1FGO-CSE and 2FGO-CSE, respectively. The previous electrolyte containing 0.5 wt% FGO (FGO-CSE) is also included for comparison. Fig. 9a shows the EIS data of the various CSE layers, from which the ionic conductivities of FGO-CSE, 1FGO-CSE, and 2FGO-CSE are determined as 8.8×10^{-4}, 9.4×10^{-4}, and 8.7×10^{-4} S cm^{-1}, respectively. An increase in FGO content up to 1 wt% may reduce the crystallinity of the polymer matrix and enhance the interactions between the FGO nanosheets and LiTFSI salt, leading to the optimal ionic conductivity. Further increasing the FGO concentration to 2 wt% leads to a deterioration in conductivity. Direct visualization of FGO agglomeration is technically challenging because the FGO is embedded within the polymer matrix and compositionally overlaps with the fluorine-containing polymer and Li salt. However, a nonuniform fluorine distribution is observed across the 2FGO-CSE layer (Fig. S14), leading to morphological inhomogeneity. This irregular microstructure gives rise to locally over-condensed regions that are unfavorable for efficient Li^+ transport. As a result, the beneficial effects of the FGO fillers are diminished. Fig. 9b and c shows

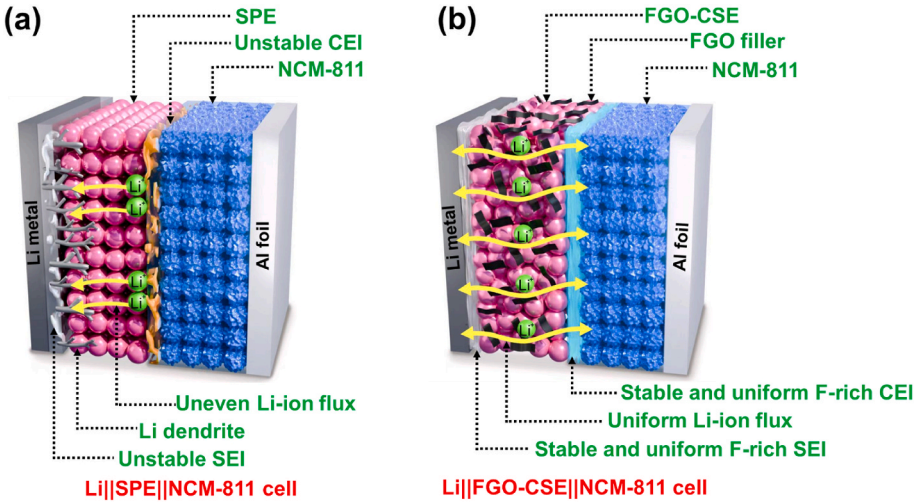

Fig. 8. Schematic illustration of charge-discharge properties of (a) Li||SPE||NCM-811 and (b) Li||FGO-CSE||NCM-811 cells.

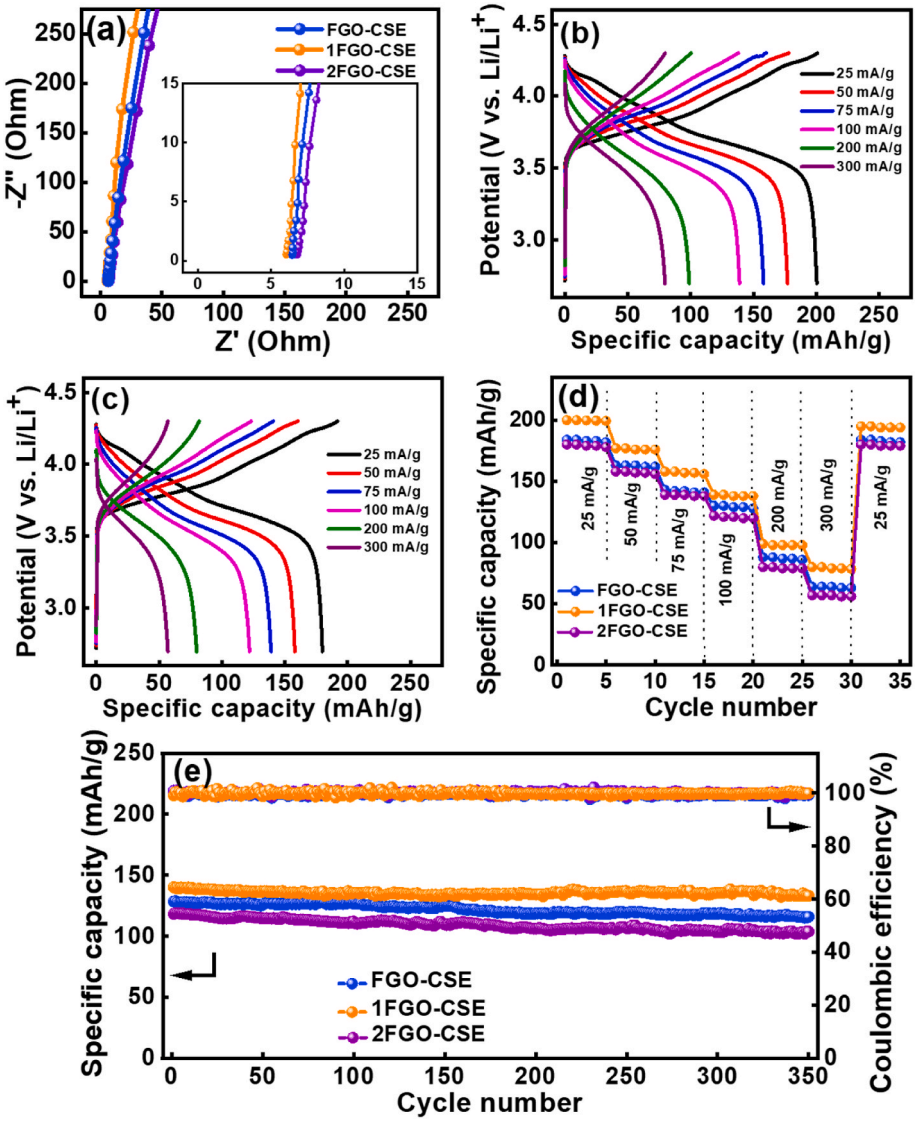

Fig. 9. (a) EIS conductivity measurement data of FGO-CSE, 1FGO-CSE, and 2FGO-CSE. Galvanostatic charge-discharge curves of (b) Li||1FGO-CSE||NCM-811 and (c) Li||2FGO-CSE||NCM-811 cells. (d) Comparative rate performance and (e) cycling stability data (measured at 100 mA g^{-1}) of various cells.

the charge-discharge curves of the Li||1FGO-CSE||NCM-811 and Li||2FGO-CSE||NCM-811 cells. Fig. 9d compares the rate capability of cells with different FGO-CSE layers, with the Li||1FGO-CSE||NCM-811 cell exhibiting the most favorable performance. In this cell, the NCM-811 cathode delivers a specific capacity of 200 mAh g^{-1} at 25 mA g^{-1}. At 300 mA g^{-1}, the capacity remains at 80 mAh g^{-1}, corresponding to 40% retention relative to the value at 25 mA g^{-1} (Table 1). Fig. 9e presents the cycling stability data of the FGO-CSE, 1FGO-CSE and 2FGO-CSE cells, which retain 90%, 95%, and 88% of their capacities, respectively, after 350 charge-discharge cycles. With 1 wt% FGO uniformly dispersed in the CSE, both the anode and cathode interfaces are effectively reinforced, which reduces the degradation of the electrodes and electrolyte, thereby mitigating capacity loss during cycling. This study demonstrates that appropriate functionalization and an optimized content of 2D carbon fillers in the CSE can significantly enhance the performance of SSLMBs. Table S3 shows that 1FGO-CSE exhibits excellent ionic conductivity even at 25 °C, while the specific capacity, rate capability, and cycle life of the proposed SSLMB rank among the best reported in the literature. These findings provide a strategy for engineering high-performance CSEs and offer valuable guidance for the advancement of next-generation solid-state energy storage devices.

3. Conclusions

In this study, we successfully developed air-stable and scalable inert functionalized graphene fillers, which were incorporated into PVDF-HFP/PPC-based SPEs to enhance the performance of SSLMBs. The effects of graphene surface functional groups on polymer-filler interactions and the resulting CSE performance were systematically investigated. Among the samples, the FGO-containing CSE exhibited the most favorable properties. The incorporation of FGO rendered the polymer matrix more interconnected and less crystalline. The FGO-CSE exhibited excellent mechanical flexibility, high thermal stability (with major degradation occurring above ~320 °C), and an extended ESW of up to ~4.8 V. The atomistic-level analyses, including DFT and AIMD calculations, revealed that FGO strongly attracted $TFSI^-$ anions, thereby facilitating Li salt dissociation and enhancing t_{Li}^+. Bader charge analysis and PEL mapping confirmed these findings, leading to an exceptional Li^+ conductivity of 9.4×10^{-4} S cm^{-1} at 25 °C for FGO-CSE. In addition, the FGO-CSE promoted the formation of LiF- and CF_x/CF_y-enriched SEI and CEI layers, which effectively suppressed parasitic side reactions, protected both the Li and NCM-811 electrodes, and enhanced their redox reversibility. Electrochemical evaluation of the Li||1FGO-CSE||NCM-811 cell demonstrated a high specific capacity of 200 mAh g^{-1} at

25 mA g^{-1} and 25 °C, along with good rate capability and excellent cycling stability, retaining 95% of its capacity after 350 cycles. Overall, this work demonstrates that incorporating functionalized 2D carbon fillers, particularly FGO, can substantially enhance the properties of the CSE. This study provides a facile and effective strategy to improve the charge-discharge performance of SSLMBs.

CRediT authorship contribution statement

Ananya Panda: Writing – original draft, Visualization, Methodology, Investigation, Formal analysis, Data curation, Conceptualization. **Jui-Cheng Kao:** Writing – original draft, Software, Methodology, Investigation, Formal analysis, Data curation, Conceptualization. **Jagabandhu Patra:** Writing – original draft, Investigation, Formal analysis, Conceptualization. **Chun-Wei Pao:** Validation, Software, Resources, Investigation, Data curation. **Chun-Chen Yang:** Writing – review & editing, Visualization, Validation, Methodology, Conceptualization. **Chien-Te Hsieh:** Writing – review & editing, Visualization, Validation. **Fu-Ming Wang:** Writing – review & editing, Validation. **Wei-Ren Liu:** Writing – review & editing, Validation. **Ju Li:** Writing – review & editing, Visualization, Validation. **Ching-Yuan Su:** Writing – review & editing, Visualization, Validation, Supervision, Resources. **Yu-Chieh Lo:** Writing – review & editing, Validation, Supervision, Software, Resources, Conceptualization. **Jeng-Kuei Chang:** Writing – review & editing, Visualization, Validation, Supervision, Resources, Project administration, Funding acquisition, Conceptualization.

Declaration of competing interest

The authors declare that they have no known competing financial interests or personal relationships that could have appeared to influence the work reported in this paper.

Acknowledgments

The authors are grateful for the financial support from the National Science and Technology Council (NSTC), Taiwan. Y.C.L. and C.W.P. thank the National Center for High-performance Computing (NCHC) for providing computational and storage resources. Y.C.L. also thanks the Center for Advanced Semiconductor Technology Research under Higher Education Sprout Project of Ministry of Education (MOE), Taiwan. In addition, J.*P.* and J.K.C. are grateful for the financial support from the Sustainable Electrochemical Energy Development (SEED) Center funded by the MOE of Taiwan.

Appendix A. Supplementary data

Supplementary data to this article can be found online at https://doi.org/10.1016/j.compositesb.2026.113503.

Data availability

Data will be made available on request.

References

[1] Randau S, Weber DA, Kotz O, Koerver R, Braun P, Weber A, Tiffee EI, Adermann T, Kulisch J, Zeier WG, Richter FH, Janek J. Benchmarking the performance of all-solid-state lithium batteries. Nat Energy 2020;5:259. https://doi.org/10.1038/s41560-020-0565-1.

[2] Xiao Y, Wang Y, Bo SH, Kim JC, Miara LJ, Ceder G. Understanding interface stability in solid-state batteries. Nat Rev Mater 2020;5:105. https://doi.org/10.1038/s41578-019-0157-5.

[3] Huang J, Li C, Jiang D, Gao J, Cheng L, Li G, Luo H, Xu ZL, Shin DM, Wang Y, Lu Y, Kim Y. Solid-state electrolytes for lithium metal batteries: state-of-the-art and perspectives. Adv Funct Mater 2024;25:2411171. https://doi.org/10.1002/adfm.202411171.

[4] Liang Y, Wu W, Li D, Wu H, Gao C, Chen Z, Ci L, Zhang J. Highly stable lithium metal batteries by regulating the lithium nitrate chemistry with a modified eutectic electrolyte. Adv Energy Mater 2022;12:2202493. https://doi.org/10.1002/aenm.202202493.

[5] Zhang S, Xiao S, Li D, Liao J, Ji F, Liu H, Ci L. Commercial carbon cloth: an emerging substrate for practical lithium metal batteries. Energy Storage Mater 2022;48:172. https://doi.org/10.1016/j.ensm.2022.03.014.

[6] Alsac EP, Nelson DL, Yoon SG, Cavallara KA, Wang C, Sandoval SE, Eze UD, Jeong WJ, McDowell MT. Characterizing electrode materials and interfaces in solid-state batteries. Chem Rev 2025;125:2009. https://doi.org/10.1021/acs.chemrev.4c00584.

[7] Janek J, Zeier WG. Challenges in speeding up solid-state battery development. Nat Energy 2023;8:230. https://doi.org/10.1038/s41560-023-01208-9.

[8] Zeng X, Liu X, Zhu H, Zhu J, Lan J, Yu Y, Lee YS, Yang X. Adv. Advanced crosslinked solid polymer electrolytes: molecular architecture, strategies, and future perspectives. Energy Mater 2024;14:2402671. https://doi.org/10.1002/aenm.202402671.

[9] Fan LZ, He H, Nan CW. Tailoring inorganic–polymer composites for the mass production of solid-state batteries. Nat Rev Mater 2021;6:1003. https://doi.org/10.1038/s41578-021-00320-0.

[10] Famprikis T, Canepa P, Dawson JA, Islam MS, Masqueiler C. Fundamentals of inorganic solid-state electrolytes for batteries. Nat Mater 2019;18:1278. https://doi.org/10.1038/s41563-019-0431-3.

[11] Zhang D, Meng X, Hou W, Hu W, Mo J, Yang T, Zhang W, Fan Q, Liu L, Jiang B, Chu L, Li M. Solid polymer electrolytes: ion conduction mechanism and enhancement strategies. Nano Res Energy 2023;2:e9120050. https://doi.org/10.26599/NRE.2023.9120050.

[12] Li S, Zhang SQ, Shen L, Liu Q, Ma JB, Lv W, He YB, Yang QH. Progress and perspective of ceramic/polymer composite solid electrolytes for lithium batteries. Adv Sci 2020;7:1903088. https://doi.org/10.1002/advs.201903088.

[13] Zheng Y, Yao Y, Ou J, Li M, Luo D, Dou H, Li Z, Amine K, Yu A, Chen Z. A review of composite solid-state electrolytes for lithium batteries: fundamentals, key materials and advanced structures. Chem Soc Rev 2020;49:8790. https://doi.org/10.1039/D0CS00305K.

[14] Yang Y, Liu J, Pei N, Chen Z, Li R, Fu L, Zhang P, Zhao J. The critical role of fillers in composite polymer electrolytes for lithium battery. Nano-Micro Lett 2023;15:74. https://doi.org/10.1007/s40820-023-01051-3.

[15] Shen Z, Cheng Y, Sun S, Ke X, Liu L, Shi Z. The critical role of inorganic nanofillers in solid polymer composite electrolyte for Li^+ transportation. Carbon Energy 2021;3:482. https://doi.org/10.1002/cey2.108.

[16] Liu S, Liu W, Ba D, Zhao Y, Ye Y, Li Y, Liu J. Filler-integrated composite polymer electrolyte for solid-state lithium batteries. Adv Mater 2022;35:2110423. https://doi.org/10.1002/adma.202110423.

[17] Miao X, Guan S, Ma C, Li L, Nan CW. Role of interfaces in solid-state batteries. Adv Mater 2023;35:2206402. https://doi.org/10.1002/adma.202206402.

[18] Zheng F, Li C, Li Z, Cao X, Luo H, Liang J, Zhao X, Kong J. Advanced composite solid electrolytes for lithium batteries: filler dimensional design and ion path optimization. Small 2023;19:2206355. https://doi.org/10.1002/smll.202206355.

[19] Peng N, Kou W, Wu W, Guo S, Wang Y, Wang J. Laminar composite solid electrolyte with poly(ethylene oxide)-threaded metal-organic framework nanosheets for high-performance all-solid-state lithium battery. Energy Environ Mater 2023;6:e12280. https://doi.org/10.1002/eem2.12280.

[20] Sand SC, Rupp JLM, Yildiz B. A critical review on Li-ion transport, chemistry and structure of ceramic–polymer composite electrolytes for solid state batteries. Chem Soc Rev 2025;54:178. https://doi.org/10.1039/D4CS00214H.

[21] Grundish NS, Goodenough JB, Khani H. Designing composite polymer electrolytes for all-solid-state lithium batteries. Curr Opin Electrochem 2021;30:100828. https://doi.org/10.1016/j.coelec.2021.100828.

[22] Yu X, Manthiram A. A review of composite polymer-ceramic electrolytes for lithium batteries. Energy Storage Mater 2021;34:282. https://doi.org/10.1016/j.ensm.2020.10.006.

[23] Subhani T, Khademolqorani S, Banitaba SN, Ramadan M, Khaliq A, Chaudhry IA, Osman AI. Advancements in battery materials: bio-based and mineral fillers for next-generation solid polymer electrolytes. ACS Appl Mater Interfaces 2024;16:63089. https://doi.org/10.1021/acsami.4c11214.

[24] Shi Y, Wen L, Yang H, Sun Z, Li F. Carbon-based materials for more reliable solid-state Li batteries. J Mater Chem A 2025;13:36803. https://doi.org/10.1039/D5TA04266F.

[25] Lan X, Luo N, Li Z, Peng J, Cheng HM. Status and prospect of two-dimensional materials in electrolytes for all-solid-state lithium batteries. ACS Nano 2024;18:9285. https://doi.org/10.1021/acsnano.4c00128.

[26] Pervez SA, Madinehei M, Moghimian N. Graphene in solid-state batteries: an overview. Nanomaterials 2022;12:2310. https://doi.org/10.3390/nano12132310.

[27] Zhai P, Yang Z, Wei Y, Guo X, Gong Y. Two-dimensional fluorinated graphene reinforced solid polymer electrolytes for high-performance solid-state lithium batteries. Adv Energy Mater 2022;12:2200967. https://doi.org/10.1002/aenm.202200967.

[28] Wang Z, Yang H, Li S, Tong H, Xu W, Zhao Y, Li L. Small components play a big role - fillers in composite solid-state electrolytes for lithium metal batteries. Energy Mater 2024;4:400080. https://doi.org/10.20517/energymater.2024.57.

[29] Georgakilas V, Tiwari JN, Kemp KC, Perman JA, Bourlinos AB, Kim KS, Zboril R. Noncovalent functionalization of graphene and graphene oxide for energy materials, biosensing, catalytic, and biomedical applications. Chem Rev 2016;116:5465. https://doi.org/10.1021/acs.chemrev.5b00620.

[30] Yan JA, Chou MY. Oxidation functional groups on graphene: structural and electronic properties. Phys Rev B 2010;82:125403. https://doi.org/10.1103/PhysRevB.82.125403.

[31] Jia W, Li Z, Wu Z, Wang L, Wu B, Wang Y, Cao Y, Li J. Graphene oxide as a filler to improve the performance of PAN-$LiClO_4$ flexible solid polymer electrolyte. Solid State Ionics 2018;315:7. https://doi.org/10.1016/j.ssi.2017.11.026.

[32] Wen J, Zhao Q, Jiang X, Ji G, Wang R, Lu G, Long J, Hu N, Xu C. Graphene oxide enabled flexible PEO-based solid polymer electrolyte for all-solid-state lithium metal battery. ACS Appl Energy Mater 2021;4:3660. https://doi.org/10.1021/acsaem.1c00090.

[33] Zhang LK, Xu HM, Jing MX, Li LX, Yang H, Shen XQ. Solid electrolyte/lithium anodes stabilized by reduced graphene oxide interlayers: implications for solid-state lithium batteries. ACS Appl Nano Mater 2021;4:9471. https://doi.org/10.1021/acsanm.1c01932.

[34] Shim J, Kim DG, Kim HJ, Lee JH, Baik JH, Lee JC. Novel composite polymer electrolytes containing poly(ethylene glycol)-grafted graphene oxide for all-solid-state lithium-ion battery applications. J Mater Chem A 2014;2:13873. https://doi.org/10.1039/C4TA02667E.

[35] Yang Z, Sun Z, Liu C, Li Y, Zhou G, Zuo S, Wang J, Wu W. Lithiated nanosheets hybridized solid polymer electrolyte to construct Li^+ conduction highways for advanced all-solid-state lithium battery. J Power Sources 2021;484:229287. https://doi.org/10.1016/j.jpowsour.2020.229287.

[36] Hu Z, Zhang X, Liu J, Zhu Y. Ion liquid modified GO filler to improve the performance of polymer electrolytes for Li metal batteries. Front Chem 2020;8:232. https://doi.org/10.3389/fchem.2020.00232.

[37] Bao W, Hu Z, Wang Y, Jiang J, Huo S, Fan W, Chen W, Jing X, Long X, Zhang Y. Poly(ionic liquid)-functionalized graphene oxide towards ambient temperature operation of all-solid-state PEO-based polymer electrolyte lithium metal batteries. Chem Eng J 2022;437:135420. https://doi.org/10.1016/j.cej.2022.135420.

[38] Ye YS, Tseng CY, Shen WC, Wang JS, Chen KJ, Cheng MY, Rick J, Huang YJ, Chang FC, Hwang BJ. A new graphene-modified protid ionic liquid-based composite membrane for solid polymer electrolytes. J Mater Chem 2011;21:10448. https://doi.org/10.1039/C1JM11152C.

[39] Shen Z, Huang J, Yang Y, Xie Y, Alodhayb AN, Wang Y, Liu Y, Shao M, Li C, Sun Y, Xu X, Shi Z. In situ construction of fluorinated graphene-modified gel polymer electrolyte for lithium metal batteries. J Power Sources 2025;629:236060. https://doi.org/10.1016/j.jpowsour.2024.236060.

[40] Shim J, Kim HJ, Kim BG, Kim YS, Kim DG, Lee JC. 2D boron nitride nanoflakes as a multifunctional additive in gel polymer electrolytes for safe, long cycle life and high rate lithium metal batteries. Energy Environ Sci 2017;10:1911. https://doi.org/10.1039/C7EE01095H.

[41] Rasul MG, Cheng M, Jiang Y, Pan Y, Yassar RS. Direct ink printing of PVdF composite polymer electrolytes with aligned BN nanosheets for lithium-metal batteries. ACS Nanosci Au 2022;2:297. https://doi.org/10.1021/acsnanoscienceau.1c00056.

[42] Chen CY, Pu NW, Liu YM, Chen LH, Wu CH, Cheng TY, Lin MH, Ger MD, Gong YJ, Peng YY, Grubb PM, Chen RT. Microwave absorption properties of holey graphene/silicone rubber composites. Compos B Eng 2018;135:119. https://doi.org/10.1016/j.compositesb.2017.10.001.

[43] Loh KP, Bao Q, Eda G, Chhowalla M. Graphene oxide as a chemically tunable platform for optical applications. Nat Chem 2010;2:1015. https://doi.org/10.1038/nchem.907.

[44] Chen X, Wang X, Fang D. A review on C1s XPS-spectra for some kinds of carbon materials, Fuller. Nanotub. Carbon Nanostruct 2020;28:1048. https://doi.org/10.1080/1536383X.2020.1794851.

[45] Zhao FG, Zhao G, Liu XH, Ge CW, Wang JT, Li BL, Wang QG, Li WS, Chen QY. Fluorinated graphene: facile solution preparation and tailorable properties by fluorine-content tuning. J Mater Chem A 2014;2:8782. https://doi.org/10.1039/C4TA00847B.

[46] Nair RR, Ren W, Jalil R, Riaz I, Kravets VG, Britnell L, Blake P, Schedin F, Mayorov AS, Yuan S, Katsnelson MI, Cheng HM, Strupinski W, Bulusheva LG, Okotrub AV, Grigorieva IV, Grigorenko AN, Novoselov KS, Geim AK. Fluorographene: a two-dimensional counterpart of teflon. Small 2010;6:2877. https://doi.org/10.1002/smll.201001555.

[47] Ho KI, Huang CH, Liao JH, Zhang W, Li LJ, Lai CS, Su CY. Fluorinated graphene as high performance dieletric materials and the application for graphene nanoelectronics. Sci Rep 2014;4:5893. https://doi.org/10.1038/srep05893.

[48] Zhang C, Huang R, Wang P, Wang Y, Zhou Z, Zhang H, Wu Z, Li L. Highly compressible, thermally conductive, yet electrically insulating fluorinated graphene aerogel. ACS Appl Mater Interfaces 2020;12:58170. https://doi.org/10.1021/acsami.0c19628.

[49] Jorio A, Dresselhaus MS, Saito R, Dresselhaus G. Raman spectroscopy in graphene-related systems. Weinheim, Germany: Wiley-VCH; 2011.

[50] Kawamura T, Okada S, Yamaki JI. Decomposition reaction of $LiPF_6$-based electrolytes for lithium ion cells. J Power Sources 2006;156:547. https://doi.org/10.1016/j.jpowsour.2005.05.084.

[51] Lan J, Zhong Y, Peng H, Meng ZD, He NX, Lan SZ, Huang L, Sun SG, Deng YP. Constructing an anion-capturing interface to achieve Li^+ cross-phase transport in composite solid electrolytes. Nat Commun 2026;17:376. https://doi.org/10.1038/s41467-025-67065-0.

[52] Zeng Y, Zhao L, Zhang J, Li Q, Sun D, Ren Y, Tang Y, Jin G, Wang H. La_2O_3 filler's stabilization of residual solvent in polymer electrolyte for advanced solid-state lithium metal batteries. Small Sci 2023;3:2300017. https://doi.org/10.1002/smsc.202300017.

[53] Sashmitha K, Anand S, Vijaya B, Santhosh N, Manohar D, Rani MU. Tailoring physical, electrochemical, mechanical and thermal properties of PPC-PVdF blend electrolyte: a synergistic effect of LIBOB salt and EC plasticizer. Results Eng 2025;26:104896. https://doi.org/10.1016/j.rineng.2025.104896.

[54] McGrath LM, Jones J, Carey E, Rohan JF. Ionic liquid-based polymer gel electrolytes for use with germanium thin film anodes in lithium ion batteries. ChemistryOpen 2019;8:1429. https://doi.org/10.1002/open.201900313.

[55] Wang J, Yang K, Sun S, Ma Q, Yi G, Chen X, Wang Z, Yan W, Liu X, Cai Q, Zhao Y. Advances in thermal-related analysis techniques for solid-state lithium batteries. InfoMat 2023;5:e12401. https://doi.org/10.1002/inf2.12401.

[56] Zhang L, Dai Y, Li C, Dang Y, Zheng R, Wang Z, Wang Y, Cui Y, Arandiyan H, Shao Z, Sun H, Zhuang Q, Liu Y. Recent advances in electrochemical impedance spectroscopy for solid-state batteries. Energy Storage Mater 2024;69:103378. https://doi.org/10.1016/j.ensm.2024.103378.

[57] Deivanayagam R, Yassar RS. Electrochemical methods and protocols for characterization of ceramic and polymer electrolytes for rechargeable batteries. Batter Supercaps 2021;4:596. https://doi.org/10.1002/batt.202000221.

[58] Bruce PG, Evans J, Vincent CA. Conductivity and transference number measurements on polymer electrolytes. Solid State Ionics 1988;28–30:918. https://doi.org/10.1016/0167-2738(88)90304-9.

[59] Zhu L, Xie H, Zheng W, Zhang K. Multi-component solid PVDF-HFP/PPC/LLTO-nanorods composite electrolyte enabling advanced solid-state lithium metal batteries. Electrochim Acta 2022;435:141384. https://doi.org/10.1016/j.electacta.2022.141384.

[60] Fan K, Lai X, Zhang Z, Chai L, Yang Q, He G, Liu S, Sun L, Zhao Y, Hu Z, Wang L. Poly(vinylidene fluoride)-based dual-salt composite polymer electrolytes for superior room-temperature solid-state lithium batteries. J Power Sources 2023;580:233342. https://doi.org/10.1016/j.jpowsour.2023.233342.

[61] Wang Y, Yang X, Meng Y, Wen Z, Han R, Hu X, Sun B, Kang F, Li B, Zhou D, Wang C, Wang G. Fluorine chemistry in rechargeable batteries: challenges, progress, and perspectives. Chem Rev 2024;124:3494.

[62] Lu Y, Zhang X, Wu Y, Cheng H, Lu Y. *In situ* polymerization of fluorinated electrolytes for high-voltage and long-cycling solid-state lithium metal batteries. Ind Chem Mater 2025;3:151. https://doi.org/10.1039/D4IM00082J.

[63] Yang F, Liu Y, Liu T, Wang Y, Nai J, Lin Z, Xu H, Duan D, Yue K, Tao X. Fluorinated strategies among all-solid-state lithium metal batteries from microperspective. Small Struct 2022;4:2200122. https://doi.org/10.1002/sstr.202200122.

[64] Zhang R, Li C, Yang B, Cao R, Chen Y, Zhou X, Ding S, Yu W. Fluorinated gel polymer electrolytes for high performance lithium metal batteries: a mechanism analysis and systematic review. Sci China Chem 2025;68:4712. https://doi.org/10.1007/s11426-025-2593-1.

[65] Tang AC, Hu EH, Jia BE, Wan CB, Wen ZY, Tso S, Ju X, Yan QY. Recent fluorination strategies in solid electrolytes for high-voltage solid-state lithium-ion batteries. Rare Met 2025;44:2268. https://doi.org/10.1007/s12598-025-03244-8.

[66] Nguyen TX, Patra J, Tsai CC, Xuan WY, Chen HYT, Dyer MS, Clemens O, Li J, Majumder SB, Chang JK, Ting JM. Secondary-phase-induced charge–discharge performance enhancement of Co-free high entropy spinel oxide electrodes for Li-ion batteries. Adv Funct Mater 2023;30:2300509. https://doi.org/10.1002/adfm.202300509.

[67] Cao D, Tan C, Chen Y. Oxidative decomposition mechanisms of lithium carbonate on carbon substrates in lithium battery chemistries. Nat Commun 2022;13:4908. https://doi.org/10.1038/s41467-022-32557-w.

[68] Guo Y, Cheng J, Zeng Z, Li Y, Zhang H, Li D, Ci L. Li_2CO_3: insights into its blocking effect on Li-ion transfer in garnet composite electrolytes. ACS Appl Energy Mater 2022;5:2853. https://doi.org/10.1021/acsaem.1c03529.

[69] Jiang Y, Liu L, Liu Y, Guan J, Wang H, Zhang M, Chen L, Cao Y, Li R, Zhou Y, Zeng Q, Li Z, Liu W, Li X, Zhang L. A Novel orientation aliphatic ketone-based liquid crystal polymer electrolyte for high-voltage solid-state lithium metal batteries. Adv Funct Mater 2025;33:2502613. https://doi.org/10.1002/adfm.202502613.

[70] Patra J, Lu SX, Kao JC, Yu BR, Chen YT, Su YS, Wu TY, Bresser D, Hsieh CT, Lo YC, Chang JK. Engineering of aromatic naphthalene and solvent molecules to optimize chemical prelithiation for lithium-ion batteries. Adv Sci 2024;11:2309155. https://doi.org/10.1002/advs.202309155.

[71] Di L, Yufang C, Weiwei S, Wei X, Shuaiyu Y, Shiqiang L, Lanlan Z, Yanshuang Z, Tianyan Y, Peitao X, Chunman Z. Cathode electrolyte interface engineering by gradient fluorination for high-performance lithium rich cathode. Adv Energy Mater 2023;13:2301765. https://doi.org/10.1002/aenm.202301765.

[72] Lei Y, Xu X, Yin J, Xu J, Xi K, Wei L, Wu H, Jiang S, Gao Y. LiF-rich electrode–electrolyte interfaces enabled by bifunctional electrolyte additive to achieve high-performance $Li/LiNi_{0.8}Co_{0.1}Mn_{0.1}O_2$ Batteries. ACS Appl Mater Interfaces 2023;15:46941. https://doi.org/10.1021/acsami.3c09641.

[73] Bai P, Ji X, Zhang J, Zhang W, Hou S, Su H, Li M, Deng T, Cao L, Liu S, He X, Xu Y, Wang C. Formation of LiF-rich cathode-electrolyte interphase by electrolyte reduction. Angew Chem, Int Ed 2022;61:e202202731. https://doi.org/10.1002/anie.202202731.